

Top of the Atmosphere Reflected Shortwave Radiative Fluxes from GOES-R

Rachel T. Pinker¹, Yingtao Ma¹, Wen. Chen¹, Istvan Laszlo², Hongqing Liu³,
Hye-Yun Kim³ and Jamie Daniels²

¹Department of Atmospheric and Oceanic Science, University of Maryland, College Park, MD

²NOAA NESDIS Center for Satellite Applications and Research, College Park, MD

³I.M. Systems Group, Inc., Rockville, MD

Correspondence to: Rachel T. Pinker (pinker@atmos.umd.edu)

Abstract. Under the GOES-R activity, new algorithms are being developed at the National Oceanic and Atmospheric Administration (NOAA)/Center for Satellite Applications and Research (STAR) to derive surface and Top of the Atmosphere (TOA) shortwave (SW) radiative fluxes from the Advanced Baseline Imager (ABI), the primary instrument on GOES-R. This paper describes a support effort in the development and evaluation of the ABI instrument capabilities to derive such fluxes. Specifically, scene dependent narrow-to-broadband (NTB) transformations are developed to facilitate the use of observations from ABI at the TOA. Simulations of NTB transformations have been performed with MODTRAN4.3 using an updated selection of atmospheric profiles and implemented with the final ABI specifications. These are combined with Angular Distribution Models (ADMs), which are a synergy of ADMs from the Clouds and the Earth's Radiant Energy System (CERES) and from simulations. Surface condition at the scale of the ABI products as needed to compute the TOA radiative fluxes come from the International Geosphere-Biosphere Programme (IGBP). Land classification at 1/6 ° resolution for 18 surface types are converted to the ABI 2-km grid over the (CONtiguous States of the United States) (CONUS) and subsequently re-grouped to 12 IGBP types to match the classification of the CERES ADMs. In the simulations, default information on aerosols and clouds is based on the ones used in MODTRAN.

27 Comparison of derived fluxes at the TOA is made with those from CERES and the level of agreement
28 for both clear and cloudy conditions is documented. Possible reasons for differences are discussed. The
29 product is archived and can be downloaded from the NOAA Comprehensive Large Array-data
30 Stewardship System (CLASS).

32 Introduction

33
34 One of the objectives at NOAA/STAR in respect to the utilization of observations from the Advanced
35 Baseline Imager (ABI) is to be able to derive shortwave (SW↓) radiative fluxes at the surface. To get to
36 the surface SW↓ from TOA satellite observations, there are two generic approaches: 1) the direct approach
37 and 2) the indirect approach. In the direct approach one uses all the necessary information needed for
38 deriving the surface fluxes (some of which can be derived from satellites). Implementation of such an
39 approach is feasible, for instance, with observations from MODIS which has a long history of product
40 availability and evaluation. Examples are illustrated in Wang and Pinker (2009), Niu and Pinker, (2015),
41 Ma et al. (2016), Pinker et al. (2018), Pinker et al., (2017a), Pinker et al. (2017b). GOES-R is a new
42 instrument and as yet, similar information to the one from MODIS is not yet available. Therefore, the
43 indirect approach is used where one starts from satellite observations at the TOA and models the
44 atmosphere and surface with best available information (which does not have to be based on ABI).
45 Examples of such an approach are discussed in Pinker, Zhang and Dutton (2005), Ma and Pinker (2012)
46 and Zhang et al. (2019). The “indirect path method” is used at the Center for Satellite Applications and
47 Research (STAR) (Laszlo et al., 2020) for deriving SW↓ radiative fluxes from satellite observations; it
48 requires knowledge of the SW broadband (0.2 – 4.0 μm) top of the atmosphere (TOA) albedo. The
49 Advanced Baseline Imager (ABI) observations onboard of the NOAA GOES-R series of satellites provide
50 reflectance in six narrow bands in the shortwave spectrum (**Table 1**); these must be first transformed into
51 broadband reflectance (the NTB conversion), and the broadband reflectance must be transformed into a
52 broadband albedo (the ADM conversion). During the pre-launch activity NTB transformations were
53 developed based on theoretical radiative transfer simulations with MODTRAN-3.7 and 14 land use

Deleted: . A satisfactory agreement between the fluxes v
observed

Deleted: have been identified.

Formatted: Font: (Default) Times New Roman

Deleted: and p

Formatted: Font: (Default) Times New Roman

Deleted: The product is archived and can be downloaded
from the NOAA Comprehensive Large Array-data
Stewardship System (CLASS) at [avl.class.noaa.gov](http://vl.class.noaa.gov), in the
"GOES-R Series ABI Products (GRABIPRD)" category
under the name of "Reflected Shortwave Radiation: TOA
¶

Deleted:

65 classifications from the International Geosphere-Biosphere Programme (*IGBP*) (Hansen et al., 2010).
66 They were augmented with ADMs from (CERES) observed ADMs (Loeb et al., 2003) and theoretical
67 simulations (Niu and Pinker, 2011) to compute TOA fluxes. The resulting NTB transformations and
68 ADMs have been tested using proxy data and simulated ABI data. The proxy instruments used in these
69 early simulations include the GOES-8 satellite, the Advanced Very-High Resolution Radiometer
70 (AVHRR) sensor on the Polar Orbiting satellites, the Spinning Enhanced Visible Infra-Red Imager
71 (SEVIRI) sensor on the European METEOSAT Second Generation (MSG) satellites, and the Moderate
72 Resolution Imaging Spectroradiometer (MODIS) instrument on the NASA Terra and Aqua Polar Orbiting
73 satellites (Pinker et al., 2021, unpublished). For each of these satellites, the evaluation of the
74 methodologies was done differently; some results were evaluated against ground observations while
75 others, against TOA information from CERES as well as from the (ESA) Geostationary Earth Radiation
76 Budget (GERB) satellite (Harries et al., 2005). The results obtained provided an insight on the expected
77 performance of the new ABI sensor. Those procedures have been subsequently updated and applied to
78 the new ABI instrument once it was built and fully characterized.

79 In this paper we describe activity in support of the effort to derive surface shortwave ($SW\downarrow$) radiative
80 fluxes from the operational Advanced Baseline Imager (ABI) instrument on the GOES-R series of the
81 NOAA geostationary meteorological satellites using the latest version of the ABI data. We describe the
82 physical basis and the development of the (NTB) transformations of satellite observed radiances and the
83 bi-directional corrections to be applied to the broadband reflectance to obtain broadband TOA albedo.
84 The methodology will be presented in section 2, data used are described in section 3, results in section 4
85 and a summary and discussion in section 5.

86

87 **2. Methodology**

88

89 The following two flowcharts (**Figs. 1 and 2**) describe the necessary steps to derive the NTB
90 transformations and the ADMs. Details on these two steps will follow.

91 The TOA narrowband and broadband reflectance can be calculated from the spectral radiances
 92 simulated from MODTRAN 4.3 and the response functions of the satellite sensor as shown in equations
 93 (1) and (2):

$$94 \quad \rho_{nb}(\theta_0, \theta, \phi) = \frac{\pi \int_{\lambda_1}^{\lambda_2} I(\lambda, \theta_0, \theta, \phi) G(\lambda) d\lambda}{\int_{\lambda_1}^{\lambda_2} \cos(\theta_0) S_0(\lambda) G(\lambda) d\lambda} \quad (1)$$

$$95 \quad \rho_{bb}(\theta_0, \theta, \phi) = \frac{\pi \int_{0.2\mu m}^{4\mu m} I(\lambda, \theta_0, \theta, \phi) d\lambda}{\int_{0.2\mu m}^{4\mu m} \cos(\theta_0) S_0(\lambda) d\lambda} \quad (2)$$

96
 97 where ρ_{nb} is narrowband reflectance; ρ_{bb} is broadband reflectance; θ_0 : solar zenith angle; θ : view
 98 (satellite) zenith angle; ϕ : relative azimuth angle;

99 I_λ : reflected spectral radiance; $S_0(\lambda)$: solar spectral irradiance;

100 G_λ : spectral response functions of satellite sensors; λ_1 and λ_2 are the spectral limits of the sensor spectral
 101 band. This approach is widely used in the scientific community as also implemented in the work of Loeb
 102 et al (2005), Wielicki et al. (2008), Su et al. (2015) and Akkermans et al. (2020).

103 As stated previously, the ADMs from CERES-based observations (Loeb et al., 2005; Kato et al. 2015)
 104 were augmented with theoretical simulations (Niu and Pinker, 2011) to compute TOA fluxes. This was
 105 done since CERES observations at that time were under-sampled. at higher latitudes.

106 The combined ADMs are developed for each angular bin by weighting the modeled and CERES ADMs
 107 based on the number of samples used to derive the ADMs of each type (Niu et al., 2011). Specifically:

108
$$\bar{R}(\theta_0, \theta, \phi) = \frac{1}{m+n} (m \times R_{CERES}(\theta_0, \theta, \phi) + n \times R_S(\theta_0, \theta, \phi)) \quad (3)$$

109 $\bar{R}(\theta_0, \theta, \phi)$: averaged ADMs at each angular bin;

110 R_{CERES} : anisotropic factor from CERES ADMs;

111 R_S : anisotropic factor from simulated ADMs;

112 m and n : observation numbers at angular bins for CERES and simulated ADMs.

113

114 2.1 Selection of Atmospheric profiles for simulations

115

116 We have selected 100 atmospheric profiles covering the globe and the seasons as input for simulations
 117 with MODTRAN4.3. The atmospheric profiles at each pressure level include temperature, water vapor
 118 and ozone. Each season includes 25 profiles. A tool was developed to select profiles from a Training Data
 119 set known as SeeBor Version 5.0 (https://cimss.ssec.wisc.edu/training_data/) (Borbas et.al. 2005).
 120 Originally it consisted of 15704 global profiles of temperature, moisture, and ozone at 101 pressure levels
 121 for clear sky conditions. The profiles are taken from NOAA-88, and the European Centre for Medium-
 122 Range Weather Forecasts (ECMWF) 60L training set, TIGR-3, ozone-sondes from 8 NOAA Climate
 123 Monitoring and Diagnostics Laboratory (CMDL) sites, and radiosondes from the Sahara Desert during
 124 2004. A technique to extend the temperature, moisture, and ozone profiles above the level of existing data
 125 was also implemented by the providers (University of Wisconsin-Madison, Space Science and
 126 Engineering Center, Cooperative Institute for Meteorological Satellite Studies (CIMSS)). **Fig. 3** shows the
 127 location of the selected profiles.

128 The SeeBor profiles are clear sky profiles. The top of the profiles is at 0.005 mb which is about 82.6 km.
 129 We did an experiment to check the impact of reducing the number of levels for a profile (initially, we
 130 have used only 40 levels). In the experiment computed were radiances from profiles with 50 levels as

131 well as radiances from profiles with 98 Levels. The difference between the two radiances (50 lev-98 lev)
132 were below 5 % reaching 15 % around 2.5 μm . In the experiment we used the odd number levels starting
133 from surface (plus the highest level) to reduce the number of profile levels. Based on these experiments
134 we have opted to keep all 98 profile levels.

135 The surface variables we have used are from MODIS and include surface skin temperature, 2 m
136 temperature, land/sea mask, and albedo. We have conducted a thorough investigation how the selected
137 profiles represent the entire sample of 15704 profiles. An example showing the comparison of
138 temperature, humidity and ozone profiles is shown in **Fig. 4**. As seen, there is a positive bias in the selected
139 profile of temperature due to their higher concentration at the lower latitudes. A positive bias can be found
140 at the lower levels while a negative bias is seen above 1 mb. Since our domain of study is in such latitudes
141 this selection should not have adverse effects on the simulations performed.

142

143 **2.2 Surface conditions**

144

145 Surface condition is one of the primary inputs into the MODTRAN simulations. The International
146 Geosphere-Biosphere Programme (IGBP) land classification is used as a source (Hansen et al., 2010;
147 Loveland et al., 2010). The dataset is at 1/6-degree resolution and includes 18 surface types. We have
148 converted the 1/6° (~18.5 km) resolution to the ABI 2-km grid using the nearest grid method (**Fig. 5**). The
149 surface type is fixed in time. The method for cloudy sky uses 4 surface types; these are also derived from
150 12 IGBP types (**Table 2**).

151

152 **2.3 Clear and cloudy sky simulations**

153

154 Under clear sky, scattering from aerosols is important. We have included 6 aerosol types (**Table 3**) to
155 cover a range of possible conditions under clear sky. Aerosol models are selected based on the type of
156 extinction and a default meteorological range for the boundary-layer aerosol models as listed below:

157 Aerosol Type 1: Rural extinction, visibility = 23 km

158 Aerosol Type 4: Maritime extinction, visibility = 23 km
159 Aerosol Type 5: Urban extinction, visibility = 5 km
160 Aerosol Type 6: Tropospheric extinction, visibility = 50 km
161 Aerosol Type 8: Advective Fog extinction, visibility = 0.2 km
162 Aerosol Type 10: Desert extinction for default wind conditions
163 For the 6 aerosol types, the total number of MODTRAN simulations for each surface type is 462,000. It
164 is obtained as follows: 6 aerosol types x 100 profiles x 770 angles.
165 When performing NTB simulations, we use all 6 types of aerosols. The Rural, Ocean, Urban and Fog
166 aerosols are distributed in the lower 0-2 km region. Tropospheric aerosol is distributed from 0 to 10 km
167 tropopause. The Rural, Ocean, Urban and Tropospheric aerosol optical properties have Relative Humidity
168 (RH) dependency. The Single Scattering Albedo (SSA) is given on 4 RH grids (0, 70, 80, 99) on a spectral
169 grid of 788 points ranging from 0.2 to 300 microns.
170 Simulations were performed for ABI for all the cloud cases described in **Table 3**. To merge cloud layers
171 with atmospheric profiles we have followed the procedure as described in *Berk et al.* (1985, 1998),
172 namely: “Cloud profiles are merged with the other atmospheric profiles (pressure, temperature, molecular
173 constituent, and aerosol) by combining and/or adding new layer boundaries. Any cloud layer boundary
174 within half a meter of an atmospheric boundary layer is translated to make the layer altitudes coincide;
175 new atmospheric layer boundaries are defined to accommodate the additional cloud layer boundaries.”
176 100% relative humidity is assumed within the cloud layers (default).

177

178 **2.4 Selection of angles**

179

180 The total number of angles used in the simulations is given in **Table 4**. The selected spectral grids for
181 solar zenith angles, satellite view angles and relative azimuth angles are at Gaussian quadrature points,
182 plus 0° to solar zenith angles (sza) and satellite viewing angles (vza) and 0° and 180° (forward and
183 backward view) to the satellite relative azimuth angles. Solar angle and satellite view angle are referenced

184 to target or surface for satellite simulation with 0° meaning looking up (zenith). Relative azimuth angle is
185 defined as when the relative azimuth angle equals 180° , the sun is in front of observer.

186 The definitions of solar zenith angle and azimuth angle in this table corresponds to the definitions of
187 MODTRAN but that is not the case for the satellite zenith angle. MODTRAN uses nadir angle as 180° -
188 satellite zenith angle, ignoring spherical geometry.

190 2.5 Selection of optimal computational scheme

191
192 MODTRAN4.3 provides three multiple scattering models (Isaacs, DISORT, and Scaled Isaacs) and three
193 band models at resolutions (1 cm^{-1} , 5 cm^{-1} , and 15 cm^{-1}). The DISORT model (Stamnes et al., 1988)
194 provides the most accurate radiance simulations but the runs are very time consuming. The Isaacs (Isaacs
195 et al. 1987) 2-stream algorithm is fast but oversimplified. The Scaled Isaacs method performs radiance
196 calculations using Isaacs 2-stream model over full spectral range and using DISORT model at a small
197 number of atmospheric window wavelengths. The multiple scattering contributions for each method are
198 identified and ratios of the DISORT and Isaacs methods are computed. This ratio is interpolated over the
199 full wavelength range, and finally, applied as a multiple scattering scale factor in a spectral radiance
200 calculation performed with the Isaacs method.

201 To optimize simulation speed and accuracy, we performed various sensitivity tests, including
202 combinations of multiple scattering models, band resolution, and number of streams. **Table 5** lists
203 simulation options and their corresponding calculation speed.

204 Based on results presented in **Table 5**, the efficient options (< 40 seconds) are Isaacs, DISORT 2-stream
205 with 15 cm^{-1} , DISORT 4-stream 15 cm^{-1} , and Scaled Isaacs all streams at all resolutions. Although the
206 ideal option is DISORT 8-stream with 1 cm^{-1} resolution, there is a trade-off between speed and accuracy.
207 **Fig. 6** compares DISORT simulated radiances at three band resolutions. We use two spectral ranges of
208 $0.4 - 0.5 \text{ }\mu\text{m}$ and $1.5 - 2.0 \text{ }\mu\text{m}$ to illustrate differences. **Fig. 6** shows that the coarser band resolution has
209 smoothed out the radiance variations. The 15 cm^{-1} has the smoothest curve among the three, and 1 cm^{-1}
210 shows more variations than the other two. Another (scientific) criteria for selecting the spectral resolution

211 is the ability to resolve/match the relative spectral response function (SRF) of a sensor. For example, the
212 SRFs of channels 1-6 of ABI are given at every 1 cm^{-1} .

213 Accordingly, we have chosen the 1 cm^{-1} band model for the MODTRAN radiance simulations. Performed
214 were also radiance simulations from different multiple scattering models at 1 cm^{-1} resolution. The whole
215 spectrum of $0.2 - 4\text{ }\mu\text{m}$ was separated to 14 sections so that the differences can be assessed clearly. For
216 wavelength below $0.3\text{ }\mu\text{m}$ and beyond 2.5 no discernible differences were found among Isaacs, DISORT
217 2-, 4-, and 8-stream, and Scaled Isaac. The largest differences occurred in the spectral range of $0.4 - 1.0$
218 μm . Scaled Isaac 8-stream follows DISORT 8-stream closely across the whole spectral range; the Scaled
219 Isaac method provided near-DISORT accuracy with the speed of Isaacs. Thus, the MODTRAN4.3
220 simulations for GOES-R ABI were set-up with Scaled Isaac 8-stream with 1 cm^{-1} band resolution.

221 For illustration, in **Fig. 7** compared are radiances simulated by Isaac 2 stream, Scaled Isaac, and DISORT-
222 4 stream for the case of Relative Azimuthal Angle= 1.9° , View Angle= 76.3° , Solar Zenith Angle= 87.2° .
223 The lines are differences between various settings and DISORT-8 stream (e.g. Isaacs minus DISORT-8).
224 Isaac has the least accuracy since it is oversimplified, 4-stream showed some improvements when
225 compared with Isaac while still has large differences for $0.4\text{ }\mu\text{m}$ and is still computationally demanding.
226 Scaled Isaac provides the smallest differences between DISORT-8. **Fig. 7** (lower) zoomed in to the large
227 difference area of $0.3\text{-}0.35\text{ }\mu\text{m}$ which indicates that Scaled Isaacs still provides satisfactory results.

229 **2.6 Regression methodologies**

231 We have derived coefficients of regression using a constrained least-square curve fitting methods of
232 Matlab, “lsqnonneg”, which can solve a linear or nonlinear least-squares (data-fitting) problem and
233 produce non-negative coefficients. Non-negative coefficients avoid generating negative TOA flux, which
234 is not a physically valid.

235 To ensure that information from all channels is used and avoid the complex cross-correlation problem, it
236 was opted to generate Narrow to Broad (NTB) coefficients for each ABI channel separately. These
237 channel specific NTB coefficients are applied to each channel to convert ABI narrow-band reflectance to

238 extended band. The final broad-band TOA reflectance is taken as the weighted sum of all 6-channel
 239 specific broad-band reflectance. The logic behind this approach is the assumption that the narrow-band
 240 reflectance from each channel is a good representative for a limited spectral region centered around the
 241 channel and the total spectral reflectance is dominated by the spectral region that contains the most solar
 242 energy.

243 To generate “separate-channel” NTB coefficients, each narrow-band ABI channel reflectance is
 244 converted to a reflectance $\rho_{bb,i}$ separately,

$$245 \quad \rho_{bb,i}(\theta_0, \theta, \phi) = c_{0,i}(\theta_0, \theta, \phi) + c_{1,i}(\theta_0, \theta, \phi) * \rho_{nb,i}(\theta_0, \theta, \phi) \quad (4)$$

246 where $\rho_{bb,i}$ is the band reflectance for an interval around each channel i ; $c_{0,i}$ and $c_{1,i}$ are regression
 247 coefficients for channel i . These regression coefficients are derived separately for various combination of
 248 surface, cloud and aerosol types. The total shortwave broad band (0.25 – 4.0 μm) reflectance ρ_{bb}^{est} is
 249 obtained by taking the weighted sum of all 6 $\rho_{bb,i}$ reflectance

$$250 \quad \rho_{bb}^{est}(\theta_0, \theta, \phi) = \sum_i \rho_{bb,i}(\theta_0, \theta, \phi) \frac{S_{0,i}}{S_0} \quad (5)$$

251 Here, S_0 and $S_{0,i}$ are total solar irradiance and band solar irradiance for each channel, respectively. Band
 252 edges around the six ABI channels are: 49980-18723, 18723-13185, 13185-9221, 9221-6812, 6812-5292,
 253 2500 cm^{-1} 0.2001-0.5341, 0.5341-0.7584, 0.7584-1.0845, 1.0845-1.4680, 1.4680-1.8896, 1.8896-4.0000
 254 μm). The corresponding solar irradiance band values are 364, 360, 287, 168, 91, 87
 255 W m^{-2} . **Fig. 8** shows the sensor response function (SRF) and locations of the six ABI channels.

256 Coefficients are generated for clear condition and 3 types of cloudy conditions. Comparison between ABI
 257 TOA flux and CERES products are shown in **Fig. 9**. The “separate-channel” coefficients work well for
 258 predominantly clear sky (**Fig.10**). Differences are somewhat more scattered for cloudy cases. The reason
 259 may be due to the fact that the ABI observation time and CERES product time do not match perfectly
 260 since cloud condition change quickly. As discussed in Gristey et al. (2019) there are SW spectral
 261 reflectance variations for different cloud types. Possibly, for ABI bands some spectral variations
 262 associated with cloud variability are missed. It is important to have the correct cloud properties to be able
 263 to select correct ADM. Misclassification of cloud properties will therefore result in flux differences. They

264 also argue that ADMs have an uncertainty due to within-scene variability and within-angular bin
265 variability leading to additional flux differences.

267 3. Data used

269 3.1 Satellite data for GOES-16 and GOES17

271 The GOES Imager data used (**Table 6**) were downloaded from
272 <https://www.avl.class.noaa.gov/saa/products/welcome>. When searching the NOAA CLASS site, go to
273 "GOES-R Series ABI Products GRABIPRD (partially restricted L1b and L2+ Data Products)". The
274 SRF are downloaded from from <https://ncc.nesdis.noaa.gov/GOESR/ABI.php>.

278 3.2 Reference data from CERES

280 The CERES Single Scanner Footprint (SSF) is a unique product for studying the role of clouds, aerosols,
281 and radiation in climate. Each CERES footprint (nadir resolution 20-km equivalent diameter) on the SSF
282 includes reflected shortwave (SW), emitted longwave (LW) and window (WN) radiances and top-of-
283 atmosphere (TOA) fluxes from CERES with temporally and spatially coincident imager-based radiances,
284 cloud properties, and aerosols, and meteorological information from a fixed 4-dimensional analysis
285 provided by the Global Modeling and Assimilation Office (GMAO). Each file in this data product
286 contains one hour of full and partial-Earth view measurements or footprints at a surface reference level.
287 Detailed information can be found via <https://ceres.larc.nasa.gov/data/#ssf-level-2> (we used version 4a).
288 Near real-time CERES fluxes and clouds in the SSF format are available within about a week of
289 observation (Kratz et al., 2014). They do not use the most recent CERES instrument calibration and thus
290 contains some uncertainty. Before GOES data were transferred to the Comprehensive Large Array-data

Deleted: <https://www.bou.class.noaa.gov/>

Formatted: Font: (Default) +Headings CS (Times New Roman)

Deleted: and the SRF from <https://ncc.nesdis.noaa.gov/GOESR/ABI.php>

Formatted: Font: (Default) Arial, Underline, Font color: Dark Red

Formatted: Left, Line spacing: single, Pattern: Clear (White)

Moved down [1]: The CODC data were not always available from CLASS and had to be obtained from NOAA/STAR temporary archives. Also, not all the required angular information needed for implementation of regressions was available online and had to be recomputed.

Deleted: .

300 Stewardship System (CLASS) system, the NOAA/STAR archive was holding new data for about a week.
301 Therefore, the initial evaluations had to be done only with data that overlapped in time. The CERES data
302 known as the FLASHFlux Level2 (FLASH_SSF) are available almost in real time from:

303 <https://ceres.larc.nasa.gov/products.php?product=FLASHFlux-Level2> (we used version 3c).

304 Due to such constraints the early comparison was done between ABI data as archived at NOAA/STAR
305 and the FLASHFlux products (in this paper, the FLASHFlux data were used only in Fig. 9). The archiving
306 of GOES-R at the NOAA Comprehensive Large Array-data Stewardship System (CLASS) started only
307 in 2019, however, it contains data starting from 2017. Once the CLASS archive became available, we
308 have augmented GOES-16 cases with observations from GOES-17; only those cases will be shown in this
309 paper.

310

311 **3.3 Data preparation**

312

313 For the re-mapping, we adopted the ESMF re-gridding package. The detailed information can be found
314 at: <http://earthsystemmodeling.org/regrid/>

315 For an ideal situation, the ABI high-resolution TOA SW fluxes should be mapped into the CERES
316 footprint for validation. However, there are reasons that make it difficult to do so. There can be more than
317 18000 pixels in a single swath of the SSF, when constrained to U.S. Different pixels have different times.
318 Neglecting the seconds, there are still more than 30 mins differences (this changes case by case) between
319 the first pixel and the one at the end and this brings up a time matching issue. By remapping the SSF to

320 ABI, we can set up a unique time for ABI (ABI is at 5 min intervals) and then constrain the region and
321 the time range of SSF.

322 Both re-mapping the ABI to SSF and remapping SSF to the ABI bring up spatial matching errors as
323 recognized by the scientific community (Rilee and Kuo, 2018; Ragulapati et al., 2021). In **Fig. 11**, we
324 show the SSF before re-gridding (**Figs 11 (a) & (b)**) and after re-gridding (**Figs. 11 (c) and (d)**). The
325 fluxes after re-mapping CERES SSF to the ABI resolution resemble well the original structure. Another
326 consideration is the computational efficiency of re-mapping the curvilinear tripolar grid to unconstructed
327 grid. For large arrays, it is more efficient to remap the unconstructed grid to the curvilinear tripolar grid.

329 **4. Results**

331 **4.1 Comparison between ABI TOA fluxes to those from CERES SSF**

332 A case for 2019/12/26 (doy 360) UTC 19:36 is illustrated in **Figs. 11-14**. Statistical summaries from an
333 extended number of cases that cover all four seasons are presented in **Table 7**.

334 We have conducted several experiments to select an appropriate regression approach to the NTB
335 transformation ensuring that non-physical results are not encountered. Based on the samples used in this
336 study (**Table 7**) the differences found for Terra and GOES-16 were in the range of -0.5-(-17.37) for bias
337 and 43.28-81.72 for standard deviation; for Terra and GOES-17 they were 11.26-47.09 and 70.25-108.73,
338 respectively. For Aqua and GOES-16 they were 7.63-33.87 and 58.68-117.43 respectively while for Aqua
339 and GOES-17 they were 0.19-31.53 and 47.55-129.42, respectively (all units are $W m^{-2}$). The evaluation
340 process revealed the challenges in undertaking such comparisons. Both estimates of TOA fluxes (CERES
341 and GOES) do no account for seasonality in the land use classification; the time matching for the different
342 satellites is important and limits the number of samples that can be used in the comparison. Based on the
343 results of this study recommendation for future work include the need to incorporate seasonality in land

344 use and spectral characteristic of the various surface types. Possible stratification by season in the
345 regressions could also be explored.

347 **4.2 Causes for differences between ABI and CERES TOA fluxes**

349 **4.2.1 Differences in surface spectral reflectance**

351 In the MODTRAN simulations we use the spectral reflectance information on various surface types as
352 provided by MODTRAN. MODTRAN version 4.3.1 contains a collection of spectral surface reflectance
353 dataset from the Moderate Spectral Atmospheric Radiance and Transmittance (MOSART) model
354 (Cornette et al., 1994) and others from Johns Hopkins University Spectral Library (Baldrige et al., 2009).
355 When doing simulation, we call the built-in surface types and use the provided surface reflectance. As
356 such, the spectral dependence of the surface reflectance used in the simulations and matched to the
357 CERES surface types may not be compatible with the classification of CERES. Also, seasonal changes
358 in surface type classification can introduce errors due to changes in the spectral surface reflectance for
359 different surface types (**Fig. 15**).

361 **4.2.2 Issues related to surface classification**

363 Another possible cause for differences between the TOA fluxes is the classification of surface types as
364 originally identified by the IGBP and used in the simulations. No seasonality is incorporated in the surface
365 type classification while such variability is part of the CERES observations.

369 **4.2.3 Issues related to match-up between GOES-R and CERES**

371 Both Terra and Aqua have sun-synchronous, near-polar circular orbits. Terra is timed to cross the equator
372 from north to south (descending node) at approximately 10:30 am local time. Aqua is timed to cross the
373 equator from south to north (ascending node) at approximately 1:30 pm local time. The periods for Terra
374 and Aqua are 99 and 98 minutes, respectively. Both have 16 orbits per day. CERES on Terra and Aqua
375 optical FOV at nadir is 16 x 32 or 20 km resolution. Terra passes CONUS during 03-06 UTC (US night
376 time), 16-20 UTC (US day time), and Aqua passes CONUS during 07-11 UTC (US night time), 18-22
377 UTC (US day time).

378 Both Terra and Aqua have an instantaneous FOV values at SWATH level. There is no perfect overlap,
379 temporally or spatially with ABI data. The ABI radiance and cloud data are on a regular grid of 2*2 km
380 over CONUS at each hour. To use CERES data for evaluation of ABI, there is a need to perform
381 collocation in both time and space.

382

383 **5. Summary**

384

385 The derivation and evaluation of TOA radiative fluxes as simulated for any given instrument are quite
386 challenging. In principle, there is a need to account for all possible changes in the atmospheric and surface
387 conditions one may encounter in the future. Yet, to know what these conditions are at the time of actual
388 observation when there is a need to select the appropriate combination of variables from the simulations,
389 is a formidable task. Differences in assumed cloud properties can also lead to differences in the fluxes
390 derived from the two instruments. Therefore, error can be expected due to discrepancies between the
391 actual conditions and the selected simulations and these are difficult to estimate. The approach we have
392 selected is based on high-quality simulations using a proven and accepted radiative transfer code
393 (MODTRAN) of known configurations and a wide range of atmospheric conditions. We have also
394 selected the best available estimates of TOA radiative fluxes from independent sources for evaluation.
395 However, the matching between different satellites in space and time is challenging. In selecting the cases
396 for evaluation, we have adhered to strict criteria of time and space coincidence as described in section
397 3.3.

398 Critical elements of an inference scheme for TOA radiative flux estimates from satellite observations are:

399 1) transformation of narrowband quantities into broadband ones;

400 2) transformation of bi-directional reflectance into albedo by applying Angular Distribution Models
401 (ADMs). In principle, the order in which these transformations are executed is arbitrary. However, since
402 well established, observation-based broadband ADMs derived from the Clouds and the Earth's Radiant
403 Energy System (CERES) project already exist, the logical procedure is to do the NTB transformation on
404 the radiances first, and then apply the ADM. This is the sequence that has been followed here. While the
405 road map to accomplish above objectives seems well defined, reaching the final goal of having a stable
406 up-to-date procedure for deriving TOA radiative fluxes from a new instrument like the ABI on the new
407 generation of GOES satellites is quite complicated. Since the final configuration of the instrument
408 becomes known at a much later stages the evaluation of new algorithms is in a fluid stage for a long time
409 so early evaluation against "ground truth" needs to be repeated frequently. Additional complication is
410 related to the lack of maturity of basic information needed in the implementation process, such as a
411 reliable cloud screened product which in itself is in a process of development and modifications. The
412 "ground truth", namely, the CERES observations are also undergoing adjustments and recalibration. As
413 such, the process of deriving best possible estimates of TOA radiative fluxes from ABI underwent
414 numerous iterations to reach its current status. An effort was made to deal the best way possible with the
415 fluid situation. All the evaluations against CERES were repeated once the ABI data reached stability and
416 were archived in CLASS and we used the most recent auxiliary information. This study sets the stage for
417 future possible improvements. One example is land classification which currently is static. Another issue
418 is related to the representation of real time aerosol optical properties which are important under clear sky
419 conditions. It is believed that only now when NOAA/STAR has a stable aerosol retrieval algorithm, it
420 would be timely to address the aerosol issue in the estimation of TOA fluxes under clear sky.

421
422
423 Data availability. The data are available upon request from the corresponding author.

424 Author contributions. The investigation and conceptualization were carried out by RTP, IL and JD. YM
425 and WC developed the software. RTP prepared the original draft. All authors contributed to the writing,
426 editing and review of the publication.

427 Competing interests. The authors declare that they have no conflict of interest.

428 Disclaimer. Publisher's note: Copernicus Publications remains neutral with regard to jurisdictional claims
429 in published maps and institutional affiliations.

430 Acknowledgements. We acknowledge the benefit from the use of the numerous data sources used in this
431 study. These include the Clouds and the Earth's Radiant Energy System (CERES) teams, the Fast
432 Longwave and Shortwave Radiative Flux (FLASHFlux) teams, the
433 University of Wisconsin-Madison, Space Science and Engineering Center, Cooperative Institute for
434 Meteorological Satellite Studies (CIMSS) for providing the SeaWiFS Version 5.0 data
435 (https://cimss.ssec.wisc.edu/training_data/), and the final versions of the GOES Imager data were
436 downloaded from <https://www.bou.class.noaa.gov/>. Several individuals have been involved in the early
437 stages of the project whose contribution led to the refinements of the methodologies. These include M.
438 M. Wonsick and Shuyan Liu. We thank the anonymous Reviewers for a very thorough and constructive
439 comments that helped to improve the manuscript. We thank the Editor Sebastian Schmidt for overseeing
440 the disposition of the manuscript.
441

442 Financial support. This research was supported by NOAA/NESDIS GOES-R Program under grants
443 5275562 1RPRP_DASR and 275562 RPRP_DASR_20 to the University of Maryland.

444

445

446 **Reference:**

- 447 Akkermans T., and Clerbaux, N.: Narrowband-to-Broadband Conversions for Top-of-Atmosphere
448 Reflectance from the Advanced Very High-Resolution Radiometer (AVHRR),
449 Remote Sens. 12 (2), 305; <https://doi.org/10.3390/rs12020305>, 2020.
- 450 Berk, A., Bernstein, L. W., and Robertson, D. C.: MODTRAN: A moderate resolution model for
451 LOWTRAN 7, Philips Laboratory, Report AFGL-TR-83-0187, Hanscom AFB, MA, 1985.
- 452 Berk, A., G. P. Anderson, P. K., Acharya, D. C. Robertson, J. H. Chetwynd, S. M. Adler-Golden:
453 MODTRAN Cloud and Multiple Scattering Upgrades with Application to AVIRIS, Remote Sensing
454 of Environment, 65 (3), 367-375, [https://doi.org/10.1016/S0034-4257\(98\)00045-5](https://doi.org/10.1016/S0034-4257(98)00045-5), 1998.
- 455 Baldrige, A. M., Hook, S. J., Grove, C. I., Rivera, G.: The ASTER spectral library version 2, Remote
456 Sensing of Environment 113, doi: 10.1016/j.rse.2008.11.007, 2009.
- 457 Borbas, E. E., Seemann, S. W., Huang, H.-L., Li, J., and Menzel, W. P.: Global profile training database
458 for satellite regression retrievals with estimates of skin temperature and emissivity. Proceedings of
459 the XIV, International ATOVS Study Conference, Beijing, China, University of Wisconsin-
460 Madison, Space Science and Engineering Center, Cooperative Institute for Meteorological Satellite
461 Studies (CIMSS), Madison, WI, pp.763-770, 2005.
- 462 Clerbaux, N., Russell, J. E., Dewitte, S., Bertrand, C., Caprion, D., De Paepe, B., Sotelino, L. G., Ipe, A.,
463 Bantges, R., and Brindley, H. E.: Comparison of GERB instantaneous radiance and flux products
464 with CERES Edition-2 data, Rem. Sens. of Environ., **113**, 102-114. doi:
465 10.1016/j.rse.2008.08.016, 2009.
- 466 Cornette, W. M., Acharya, P. K., Robertson, D. C., and Anderson, G. P.: Moderate Spectral Atmospheric
467 Radiance and Transmittance Code (*MOSART*), Rep. R-057-94 (11–30), La Jolla, CA: Photon
468 Research Associates, 1994.
- 469 Gristey, J. J., Su, W., Loeb, N. G., Vonder Haar, T. H., Tornow, F., Schmidt, K. S., Hakuba, M. Z.,

470 Pilewskie, P., Russell, J. E.: Shortwave Radiance to Irradiance Conversion for Earth Radiation
471 Budget Satellite Observations: A Review, *Remote Sens.* 13, 2640,
472 <https://doi.org/10.3390/rs13132640>, 2021.

473 Kato, S., Loeb, N. G., Rutan, D. A., Rose, F. G.: Clouds and the Earth's Radiant Energy System
474 (CERES) Data Products for Climate Research *Journal of the Meteorological Society of Japan*,
475 93 (6), 597–612, DOI:10.2151/jmsj.2015-048, 2015.

476 Kratz, D. P., Stackhouse Jr., P. W., Gupta, S. K., Wilber, A. C., Sawaengphokhai, P., and McGarragh, G.
477 R.: The Fast Longwave and Shortwave Flux (FLASHFlux) Data Product: Single-Scanner Footprint
478 Fluxes, *J. Appl. Meteor. Climatology*, 53, 1059-1079, doi: 10.1175/JAMC-D-13-061.1, 2014.

479 Hansen, M. C., Defries, R. S., Townshend, J. R. G., and Sohlberg, R.: Global land cover classification
480 at 1km spatial resolution using a classification tree approach, *International Journal of Remote*
481 *Sensing*, 21(6-7):1331 – 1364, DOI:10.1080/014311600210209
482 <https://doi.org/10.1080/014311600210209>, 2010.

483 Harries, J. E., Russell, J. E., Hanafin, J. A., Brindley, H., Futyán, J., Rufus, J., Kellock, S., G. Matthews,
484 R. Wrigley, A. Last, J. Mueller, R. Mossavati, J. Ashmall, E. Sawyer, D. Parker, M. Caldwell, P
485 M. Allan, A. Smith, M. J. Bates, B. Coan, B. C. Stewart, D. R. Lepine, L. A. Cornwall, D. R.
486 Corney, M. J. Ricketts, D. Drummond, D. Smart, R. Cutler, S. Dewitte, N. Clerbaux, L. Gonzalez,
487 A. Ipe, C. Bertrand, A. Joukoff, D. Crommelynck, N. Nelms, D. T. Llewellyn-Jones, G. Butcher,
488 G. L. Smith, Z. P. Szewczyk, P. E. Mlynchak, A. Slingo, R. P. Allan, and M. A. Ringer: The
489 Geostationary Earth Radiation Budget Project, *Bull. Amer. Meteor. Soc.* 86 (7): 945, doi:
490 10.1175/BAMS-86-7-945, 2005.

491 Isaacs, R. G., W.-C. Wang, R. D. Worsham, and S. Goldenberg, S.: Multiple scattering LOWTRAN and
492 FASCODE models. *Applied Optics*, 26(7), 1272 – 1281, 1987.

493 Kato, S., and Loeb, N. G.: Top-of-atmosphere shortwave broadband observed radiance
494 and estimated irradiance over polar regions from Clouds and the Earth's Radiant Energy System
495 (CERES) instruments on Terra, *J. Geophys. Res.*, 110, D07202,
496 doi:10.1029/2004JD005308, 2005.

497 Laszlo, I., Liu, H., Kim, H.-Y., and Pinker, R. T. : GOES-R Advanced Baseline Imager (ABI) Algorithm
498 Theoretical Basis Document (ATBD) for Downward Shortwave Radiation (Surface), and Reflected
499 Shortwave Radiation (TOA), version 3.1, Available at <https://www.goes-r.gov/resources/docs.html>,
500 2018.

501 Laszlo, I., Liu, H., Kim, H.-Y., and Pinker, R. T.: Shortwave Radiation from ABI on the GOES-R Series,
502 in: *The GOES-R Series*, edited by S. J. Goodman, T. J. Schmit, J. Daniels and R. J. Redmon. 179-191,
503 Elsevier, doi: <https://doi.org/10.1016/B978-0-12-814327-8.00015-9>, 2020.

504 Loeb, N. G., Smith, N. M., Kato, S., Miller, W. F., Gupta, S. K., Minnis, P. and Wielicki, B. A.: Angular
505 Distribution Models for Top-of Atmosphere Radiative Flux Estimation from the Mission Satellite,
506 Part I: Methodology, *Journal of Applied Meteorology*, 42 240-265, 2003.

507 Loeb N. G. et al.: Angular distribution models for top-of- atmosphere radiative flux estimation from the
508 Clouds and the Earth's Radiant Energy System Instrument on the Terra satellite. part I:
509 Methodology. *J. Atmos. Oceanic Technol.*, 22:338–351, 2005.

510 Loveland T. R., B. C. Reed, J. F. Brown, D. O. Ohlen, Z. Zhu, L. Yang, J. W. Merchant: Development
511 of a global land cover characteristics database and IGBP DISCover from 1 km AVHRR data,
512 *International Journal of Remote Sensing*, 21 (6-7), 1303-1330, 2010.

513 Ma, Y., R. T. Pinker, M. M. Wonsick, C. Li, and L. M. Hinkelman: Shortwave radiative fluxes on
514 slopes. *JAMC*, 55, 1513-1532, <https://doi.org/10.1175/JAMC-D-15-0178.1>, 2016.

515 Ma, Y. and Pinker, R. T.: Shortwave Radiative Fluxes from Satellites: An Update. *J. Geophys. Res.*
516 *Atmos.*, 117, Issue D23, DOI: 10.1029/2012JD018332, 2012.

517 Niu, X. and Pinker, R. T.: Revisiting satellite radiative flux computations at the top
518 of the atmosphere, *International Journal of Remote Sensing*, DOI:10.1080/01431161.2011.571298,
519 2011.

520 Niu, X. and Pinker, R. T.: An improved methodology for deriving high resolution
521 surface shortwave radiative fluxes from MODIS in the Arctic region, *J. Geophys. Res.*
522 *Atmos.*, 120, 2382–2393, doi: 10.1002/2014JD022151, 2015.

523 Pinker, R. T., Zhang B., Dutton E. G.: Do satellites detect trends in surface solar radiation? *SCIENCE*,
524 308, 5723, 850-854, 2005.

525 Pinker, R. T., A. Bentamy, B. Zhang, W. Chen, and Ma, Y.: The net energy budget at the ocean-
526 atmosphere interface of the “Cold Tongue” region, *J. Geophys. Res. Oceans*, 122, doi: 10.1002/
527 2016JC012581, 2017a.

528 Pinker, R. T., S. Grodsky, B. Zhang, A. Busalacchi, and Chen, W.: ENSO Impact on Surface Radiative
529 Fluxes as Observed from Space. *J. Geophys. Res.-Oceans.*, doi: 10.1002/2017JC012900, 2017b.

530 Pinker, R. T., Zhang, B. Z., Weller, R. A., and Chen, W.: Evaluating surface radiation fluxes observed
531 from satellites in the southeastern Pacific Ocean. *Geophysical Research Letters*, 45.
532 <https://doi.org/10.1002/2017GL076805>, 2018.

533 Rajulapati, C. R., S. M. Papalexiou, M. P. Clark, and Pomeroy, J. W.: The Perils of Regridding:
534 Examples Using a Global Precipitation Dataset, *Journal of Applied Meteorology and*
535 *Climatology*, 60 (11), 1561–1573, doi: 10.1175/JAMC-D-20-0259.1, 2021.

536 Rilee M. L. and Kuo, K. S.: The Impact on Quality and Uncertainty of Regridding Diverse Earth
537 Science Data for Integrative Analysis, IN43C-0916, 2018.

538 Scarino et al.: A Web-Based Tool for Calculating Spectral Band Difference Adjustment Factors Derived
539 from SCIAMACHY Hyperspectral Data, *IEEE Trans. Geo. Remote Sens.*, 54, 5,
540 10.1109/TGRS.2015.2502904, 2016.

541 Stamnes, K., S.-C. Tsay, W. Wiscombe and K. Jayaweera: Numerically stable algorithm for discrete-
542 ordinate-method radiative transfer in multiple scattering and emitting layered media, *Applied*
543 *Optics*, 27 (12), 2502–2509, 1988.

544 Su, W., Corbett, J., Eitzen, Z., and Liang, L.: Next-generation angular distribution models for
545 top-of-atmosphere radiative flux calculation from CERES instruments: methodology, *Atmos.*
546 *Meas. Tech.*, 8, 611–632, <https://doi.org/10.5194/amt-8-611-2015>, 2015.

547 Wang, H; Pinker, R. T.: Shortwave radiative fluxes from MODIS: Model development and
548 implementation. *JGR- Atmospheres*, 114, D20201, 2009.

549 Wielicki, B. A.; Doelling, D. R.; Young, D. F.; Loeb, N. G.; Garber, D. P.; MacDonnell, D. G.: Climate
550 quality broadband and narrowband solar reflected radiance calibration between sensors in orbit.
551 In Proceedings of the IGARSS 2008 IEEE International Geoscience and Remote Sensing
552 Symposium, Boston, MA, USA, 7–11 July 2008.

553 Zhang, T., Stackhouse Jr., P. W., Cox, S. J., Mikovitz, J. C., Long, C. N.: Clear-sky shortwave
554 downward flux at the Earth’s surface: Ground-based data vs. satellite-based data, *Journal of*
555 *Quantitative Spectroscopy & Radiative Transfer*, 224, 247-260, 2019,
556 www.elsevier.com/locate/jqsrt.

557
558
559
560

Tables

Table 1. Channel information and spectral bands for ABI.

<i>ABI Band #</i>	<i>Central wavelength (μm)</i>	<i>Spectral band (μm)</i>
1	VIS 0.47	0.45-0.49
2	VIS 0.64	0.60-0.68
3	NIR 0.86	0.847-0.882
4	NIR 1.38	1.366-1.380
5	NIR 1.61	1.59-1.63
6	NIR 2.26	2.22-2.27

561

562

563

564 Table 2. Surface classification description for IGBP 18 types, IGBP 12 types, CERES clear sky 6 types,
 565 and NTB cloudy sky 4 types

IGBP (18 types)	IGBP (12 types)	CERES clear-sky (6 types)	NTB cloudy-sky (4 types)
Evergreen Needleleaf	Needleleaf Forest	Mod-High Tree/Shrub	Land
Deciduous Needleleaf			
Evergreen Broadleaf	Broadleaf Forest		
Deciduous Broadleaf			
Mixed Forest	Mixed Forest		
Closed Shrublands	Closed Shrub		
Woody Savannas	Woody Savannas		
Savannas	Savannas	Low-Mod Tree/Shrub	
Grasslands	Grasslands		
Permanent Wetlands			
Tundra			
Croplands	Croplands		
Open Shrublands	Open Shrub		
Urban and Built-up	Open Shrub	Dark Desert	Desert
Bare Soil and Rocks	Barren and Desert	Bright Desert	
Snow and Ice	Snow and Ice	Snow and Ice	Snow and Ice
Water Bodies	Ocean	Ocean	Water

566
 567
 568

569

570 Table 3. The various classes for which NTB coefficients are generated.

Parameter	Clear condition	Cloudy condition
Aerosol or cloud type	6 aerosol types (rural, maritime, urban, tropospheric, fog, desert)	3 cloud types (cirrus, stratocumulus, altostratus)
Optical depth (OD)	Typical VIS (km) values for each aerosol types (no OD grid for each aerosol type). Rural: 23, maritime: 23, urban: 5, tropospheric: 50, fog: 0.2, desert: (default VIS for wind speed 10m/s)	Cirrus: [0, 0.8, 1.2, 1.8, 3.2] Stratocumulus: [0, 0.8, 1.2, 1.8, 3.2, 5.8, 8.2, 15.8, 32.2, 51.8, 124.2] Altostratus: [0, 15.0, 30.0, 50.0, 80.0]
Surface type	12 IGBP surface types	4 types (Water, Land, Desert, Snow/Ice)

571

572

573

574

575

576

577

Table 4. Angles used in simulations. To be consistent with what is presented in the ABI Shortwave Radiation Budget (SRB) Algorithm Theoretical Basis Documents (ATBD) (Laszlo et al, 2018) the additional angles used in the simulations are not given in this Table.

Angle Type	Angles
Solar Zenith Angle [°]	0.0, 12.9, 30.8, 41.2, 48.3, 56.5, 63.2, 69.5, 75.5, 81.4, 87.2
Satellite Zenith Angle [°]	0.0, 11.4, 26.1, 40.3, 53.8, 65.9, 76.3
Azimuth Angle [°]	0.0, 1.9, 10.0, 24.2, 44.0, 68.8, 97.6, 129.3, 162.9, 180

578

579

580

581

582

Table 5. MODTRAN simulation speed test (CPU MHz 2099.929).

Algorithm	Stream	Band Resolution (cm ⁻¹)	Speed (~seconds)
Isaacs	2	1	40
DISORT	2	1, 5, 15	280, 70, 30
	4	1, 5, 15	560, 120, 40
	8	1, 5, 15	930, 300, 110
Scaled	2	1, 5, 15	30, 10, 6.67
Isaac	4	1, 5, 15	30, 10, 6.67
	8	1, 5, 15	30, 10, 6.67

583

584

585

586

587

588

Table 6. Details on data used as input for calculations.

Short Name	Long Name	MODE	ABI-Channel	Scan Sector	Spatial Resolution
RadC	L1b Radiance	M6	C01-C06	CONUS	5000x3000
AODC	L2 Aerosol	M6	--	CONUS	2500x1500
ACMC	L2 Clear Sky Masks	M6	--	CONUS	2500x1500
ACTPC	L2 Cloud Top Phase	M6	--	CONUS	2500x1500
CODC*	L2 Cloud Optical Depth	M6	--	CONUS	2500x1500

589

590

591

592

593

594

*The CODC data were not always available from CLASS and had to be obtained from NOAA/STAR temporary archives. Also, not all the required angular information needed for implementation of the regressions is available online and had to be re-generated.

Moved (insertion) [1]

Deleted: was

Deleted: recomputed

597 Table 7. Statistical summary for all selected cases intercompared at instantaneous time scale.

Case	CERES	GOES-R	Corr	Bias	Std	RMSE	N
07/31 2019	Terra	G16	0.82	0.81	69.81	69.81	0.22 x10 ⁶
		G17	0.87	29.13	90.10	94.70	1.78 x10 ⁶
UTC 19	Aqua	G16	0.76	33.87	117.43	122.22	1.58 x10 ⁶
		G17	0.78	31.53	129.42	133.21	0.29 x10 ⁶
09/13 2019	Terra	G16	0.87	-17.37	81.72	83.54	0.13x10 ⁶
		G17	0.71	47.09	108.73	118.48	1.73x10 ⁶
UTC 20	Aqua	G16	0.76	18.22	108.50	110.02	1.46x10 ⁶
		G17	0.73	25.14	81.95	85.72	0.53x10 ⁶
09/21 2019	Terra	G16	0.85	6.78	66.66	67.00	0.35x10 ⁶
		G17	0.83	26.41	87.64	91.57	1.75x10 ⁶
UTC 19	Aqua	G16	0.82	29.66	105.09	109.20	1.67x10 ⁶
		G17	0.76	6.03	94.70	94.89	0.15x10 ⁶
09/30 2019	Terra	G16	0.88	4.49	64.79	64.94	0.40x10 ⁶
		G17	0.80	19.35	86.41	88.55	1.74x10 ⁶
UTC 19	Aqua	G16	0.80	19.87	100.45	102.40	1.69x10 ⁶
		G17	0.72	2.71	91.79	91.83	0.12x10 ⁶
	Terra	G16	0.86	5.84	51.44	51.77	0.35x10 ⁶

10/23		G17	0.87	22.47	70.25	73.76	1.75x10 ⁶
2019		G16	0.89	17.10	75.95	77.85	1.67x10 ⁶
UTC	Aqua	G17	0.78	8.98	72.52	73.07	0.15x10 ⁶
19		G16	0.87	-0.50	43.28	43.28	0.35x10 ⁶
11/08	Terra	G17	0.82	17.18	71.27	73.31	1.75x10 ⁶
2019		G16	0.90	10.08	71.27	71.98	1.67x10 ⁶
UTC	Aqua	G17	0.68	1.53	47.55	47.58	0.15x10 ⁶
19		G16	0.79	7.98	49.10	49.75	0.35x10 ⁶
11/24	Terra	G17	0.87	14.10	78.35	79.61	1.76x10 ⁶
2019		G16	0.82	7.63	58.68	59.17	1.67x10 ⁶
UTC	Aqua	G17	0.65	0.19	63.14	63.14	0.15x10 ⁶
19		G16	0.88	5.24	53.28	53.54	0.35x10 ⁶
12/26	Terra	G17	0.76	11.26	73.95	74.80	1.76x10 ⁶
2019		G16	0.83	9.79	58.90	59.56	1.67x10 ⁶
UTC	Aqua	G17	0.73	0.85	52.53	52.54	0.15x10 ⁶
19							

598
599
600
601
602
603
604
605
606

607 List of Figures

608 Figure 1. Flowchart of the NTB transformations illustrating the main processing sections.

609 Figure 2. Schematic illustration of the logic employed to synthesize modeled and observed ADMs.

610 Figure 3. The location of the 100 selected clear sky profiles from SeeBor used in the simulations.

611 Figure 4. Profile statistics of: (a) temperature; (b) water vapor; (c) ozone for the entire available sample
612 and for the reduced sample used in this study. Error bar is 1 standard deviation.

613 Figure 5. Re-mapped IGBP surface classifications over the CONUS at 2-km ABI grid.

614 Figure 6. Simulated Radiances from DISORT 8-stream (with 1, 5, and 15 cm^{-1} resolution band model
615 for spectral range of 0.4 – 0.5 μm (left) and 1.5 – 2.0 μm (right).

616 Figure 7. Radiance differences between various multi-scattering algorithms and DISORT-8 stream.
617 *Upper*: the whole simulated spectrum of 0.2-4 μm ; *Lower*: zoom on 0.3-0.35 μm (Relative
618 Azimuthal Angle=1.9°, View Angle=76.3°, Solar Zenith Angle=87.2°).

619 Figure 8. Locations of the six ABI channel SRFs. X-axis is wavenumber. Y-axis is solar irradiance.

620 Figure 9. Comparison of TOA flux from ABI and CERES FLASHFlux for 2017/11/25, 17:57Z. (a)
621 CERES Terra product; (b): results with “separate-channel” coefficients. (c): difference (ABI-
622 CERES); (d): histogram of ABI-CERES differences (this is the only case illustrated in this paper
623 with data from FLASHFlux)

624 Figure 10. Statistics for relative Bias and RMSE. The y-axis is percentage. The x-axis is the case used in
625 the inter-comparison. Blue - cloudy orange - clear sky and t gray - all sky.

626 Figure 11. (a) All sky TOA SW from CERES_SSF/Aqua, (b) CERES_SSF/Terra, (c) re-gridded
627 CERES_SSF/Aqua, (d) re-gridded CERES_SSF/Terra, (e) GOES-16 and (f) GOES-17 on
628 12/26/2019 at UTC 19:36.

629 Figure 12. (a) Frequency distribution of all-sky TOA SW differences between ABI on GOES-16 and
630 CERES, (b) ABI on GOES-17 and CERES_SSF using Aqua (Upper) and Terra (Lower). All
631 observations were used (clear and cloudy) on 12/26/2019 at UTC 19:36.

632 Figure 13. Same as Figure 11 but for clear TOA SW differences.

633 Figure 14. Same as Figure 11 but for cloudy TOA SW differences.

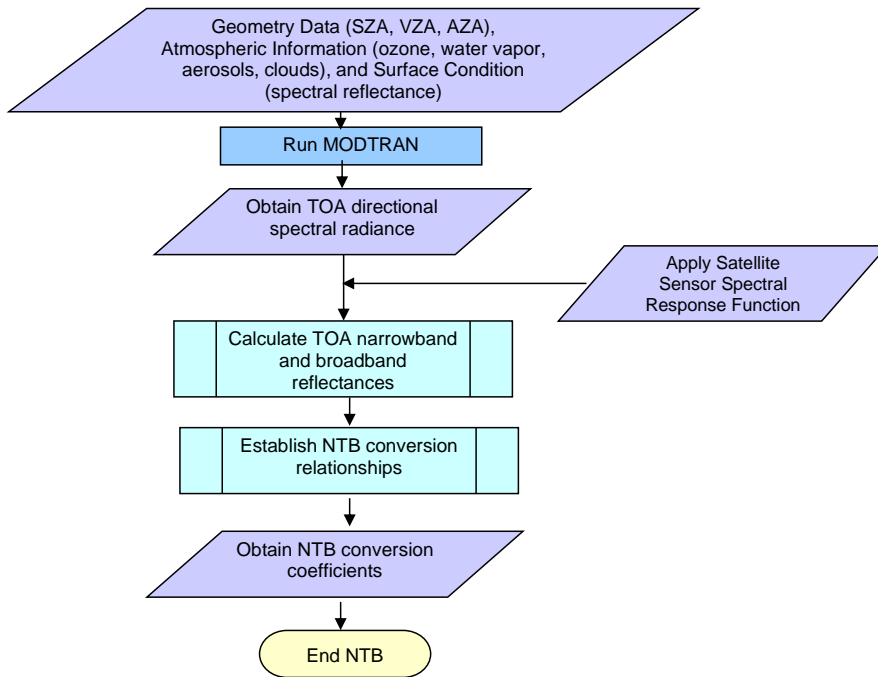
634 Figure 15. *Left:* Sensor response function for ABI channel 6; *Right:* Spectral albedo for desert and open
635 shrubs. Desert albedo value is much higher than open shrubs at 2.2 μm .

636
637
638
639
640
641
642
643
644
645
646
647
648
649
650
651
652
653
654
655
656
657
658
659
660
661
662
663
664
665
666
667
668
669

670 **Figures**

671

672

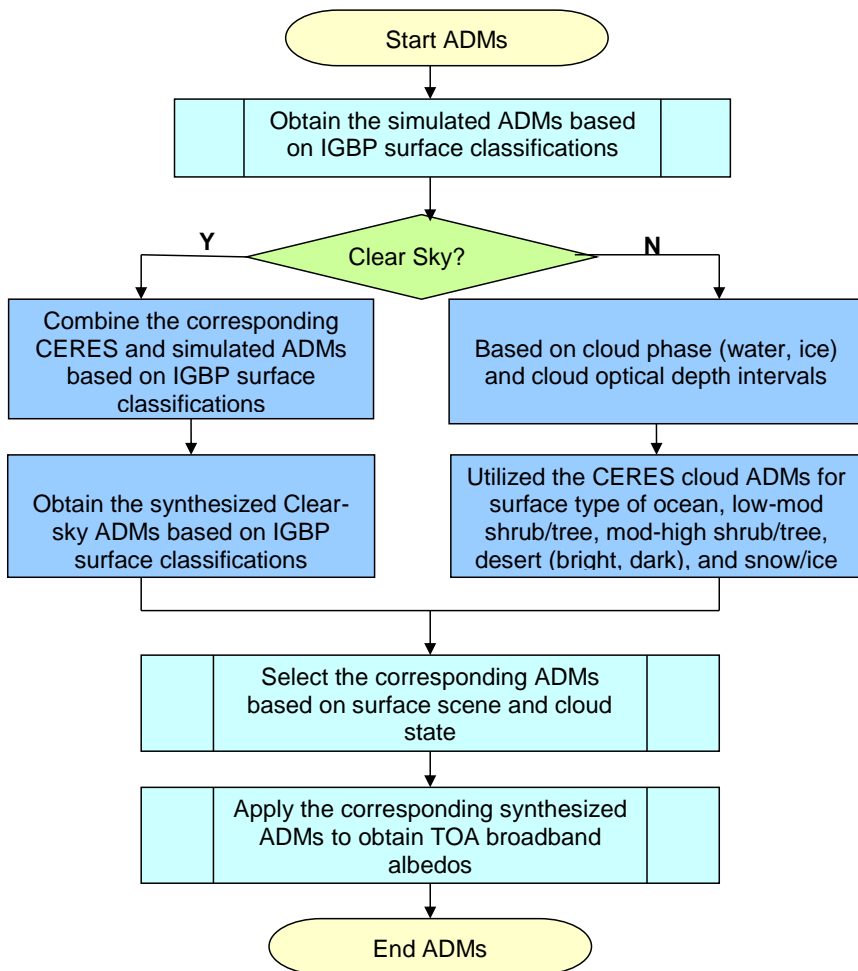


673
674 Figure 1. Flowchart of the NTB transformations illustrating the main processing sections.

675

676

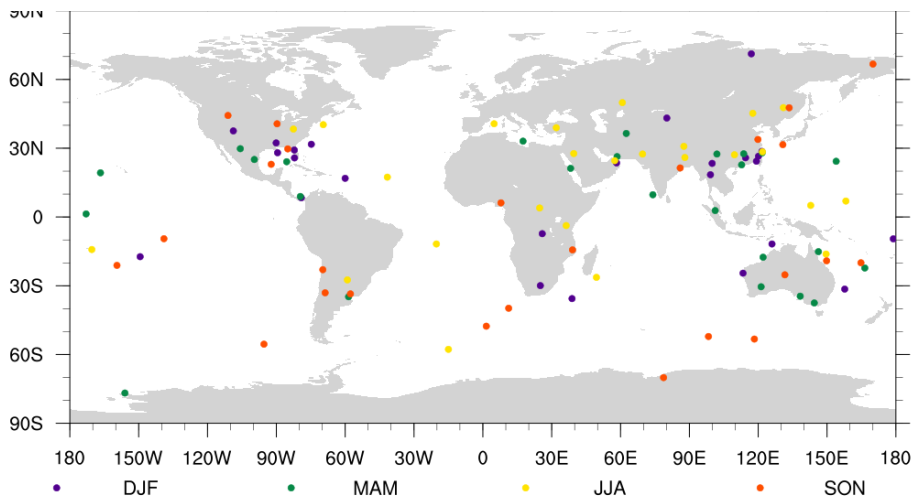
677



678

679 Figure 2. Schematic illustration of the logic employed to synthesize modeled and observed ADMs.

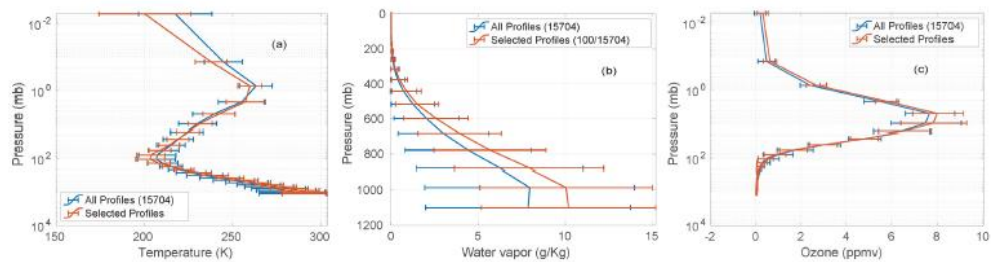
680
681
682
683



684
685
686

Figure 3. The location of the 100 selected clear sky profiles from SeeBor used in the simulations.

687



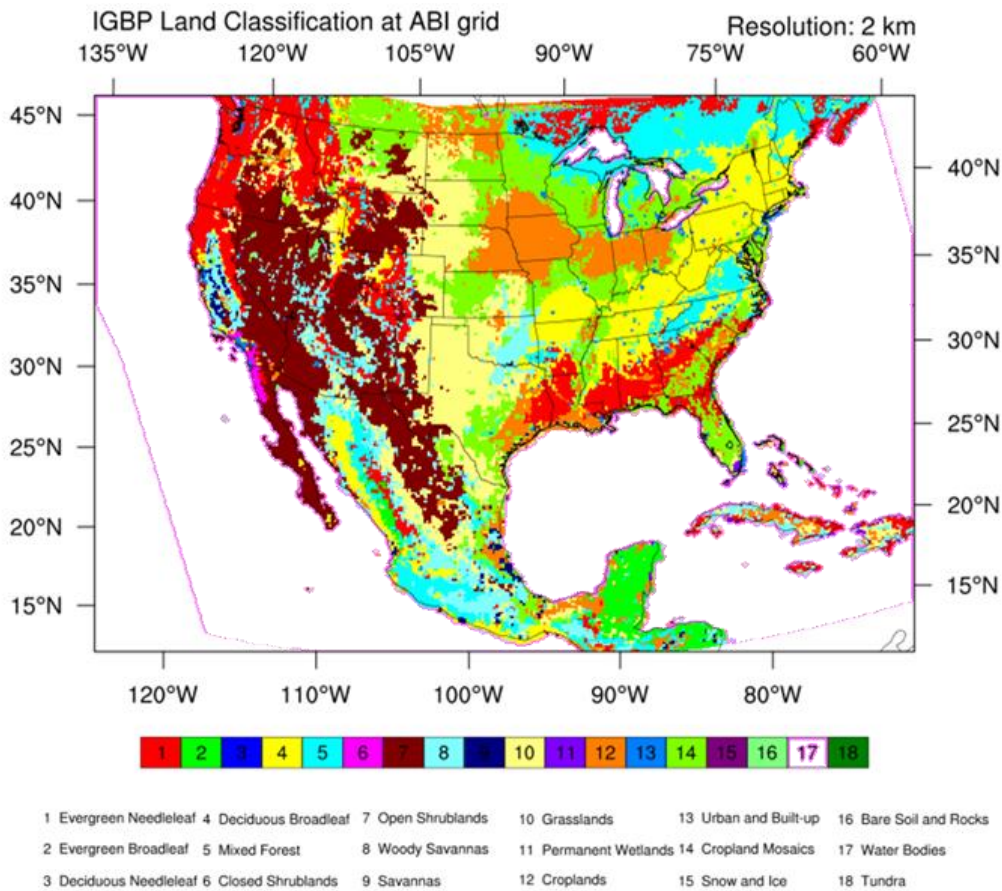
688

689 Figure 4. Profile statistics of: (a) temperature; (b): water vapor; (c) ozone for the entire available sample
690 and for the reduced sample used in this study. Error bar is 1 standard deviation.

691

692

693



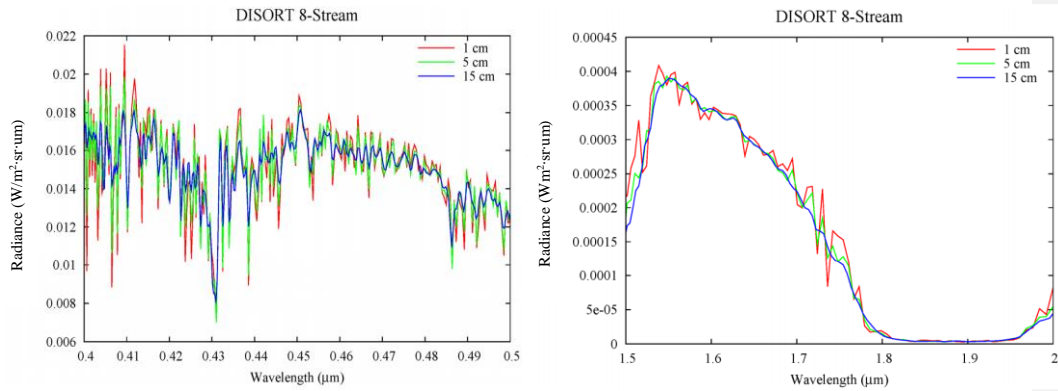
694

695 Figure 5. Re-mapped IGBP surface classifications over the CONUS at 2-km ABI grid.

696

697

698



699

700

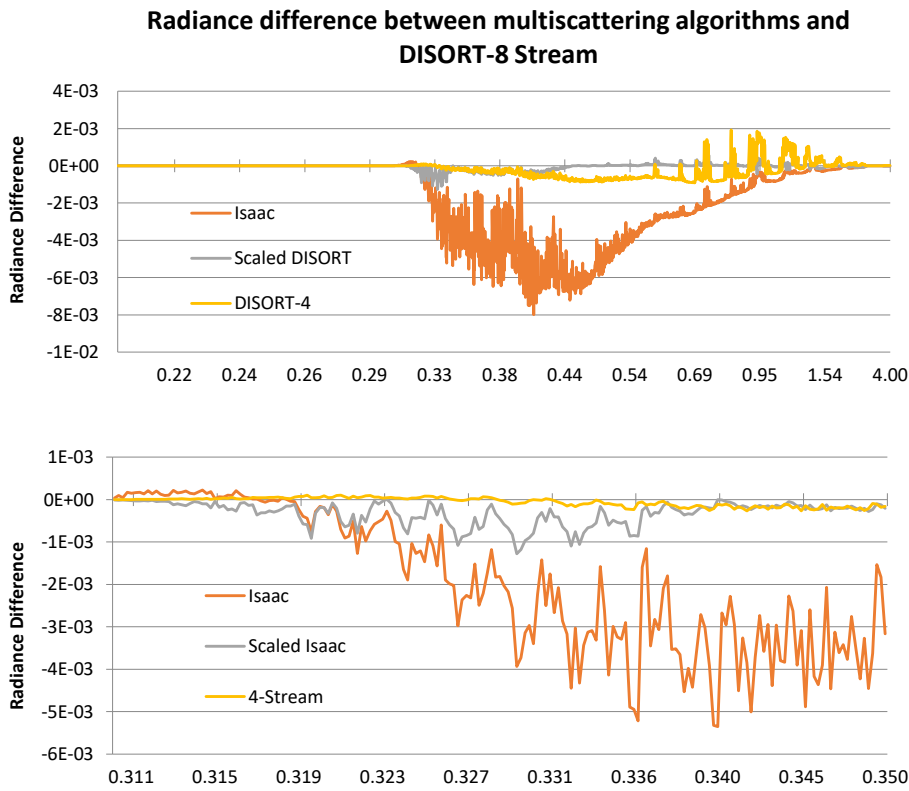
701

702

703

Figure 6. Simulated Radiances from DISORT 8-stream (with 1, 5, and 15 cm⁻¹ resolution band model for spectral range of 0.4 – 0.5 μm (left) and 1.5 – 2.0 μm (right).

704
705



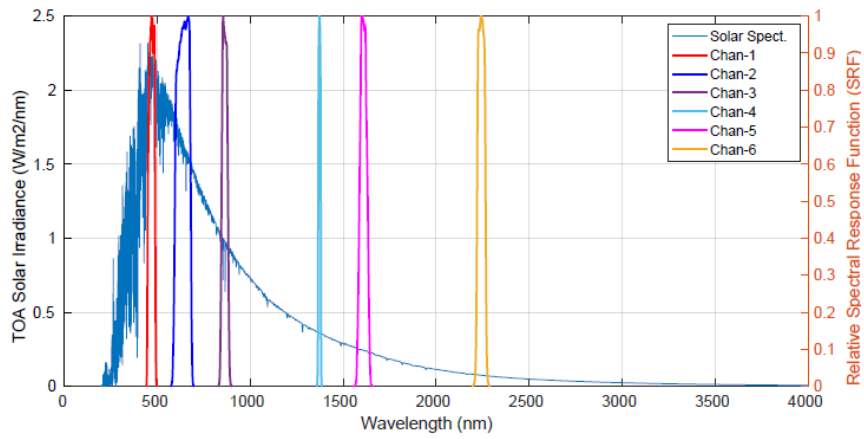
706

707

708 Figure 7. Radiance differences between various multi-scattering algorithms and DISORT-8 stream.

709 *Upper:* the whole simulated spectrum of 0.2-4 μm ; *Lower:* zoom on 0.3-0.35 μm (Relative
710 Azimuthal Angle=1.9°, View Angle=76.3°, Solar Zenith Angle=87.2°).

711



712

713

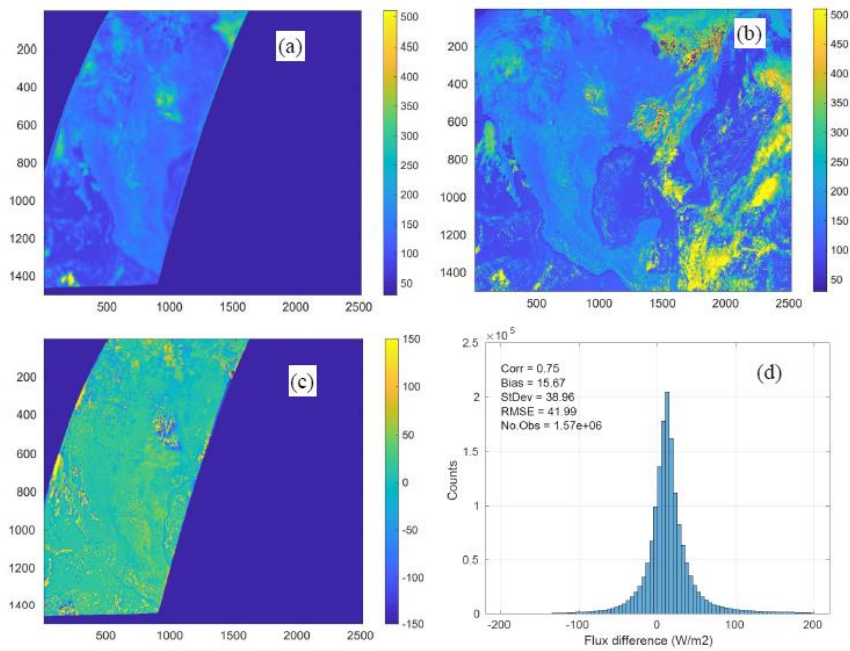
714 Figure 8. Locations of the six ABI channel SRFs. X-axis is wavenumber. Y-axis is solar irradiance.

715

716

717

718



719

720 Figure 9. Comparison of TOA flux from ABI and CERES FLASHFlux for 2017/11/25, 17:57Z. (a)

721 CERES Terra product; (b): results with “separate-channel” coefficients. (c): difference (ABI-

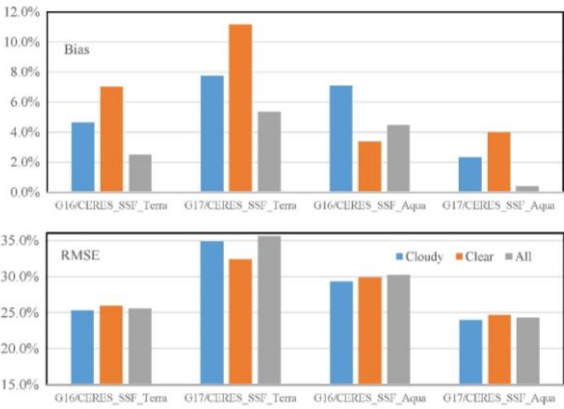
722 CERES); (d): histogram of ABI-CERES differences (this is the only case illustrated in this paper

723 with data from FLASHFlux).

724

725

726



727

728

729

Figure 10. Statistics for relative Bias and RMSE. The y-axis is percentage. The x-axis is the case used in the inter-comparison. Blue - cloudy orange - clear sky and t gray - all sky.

730

731

732

733

734

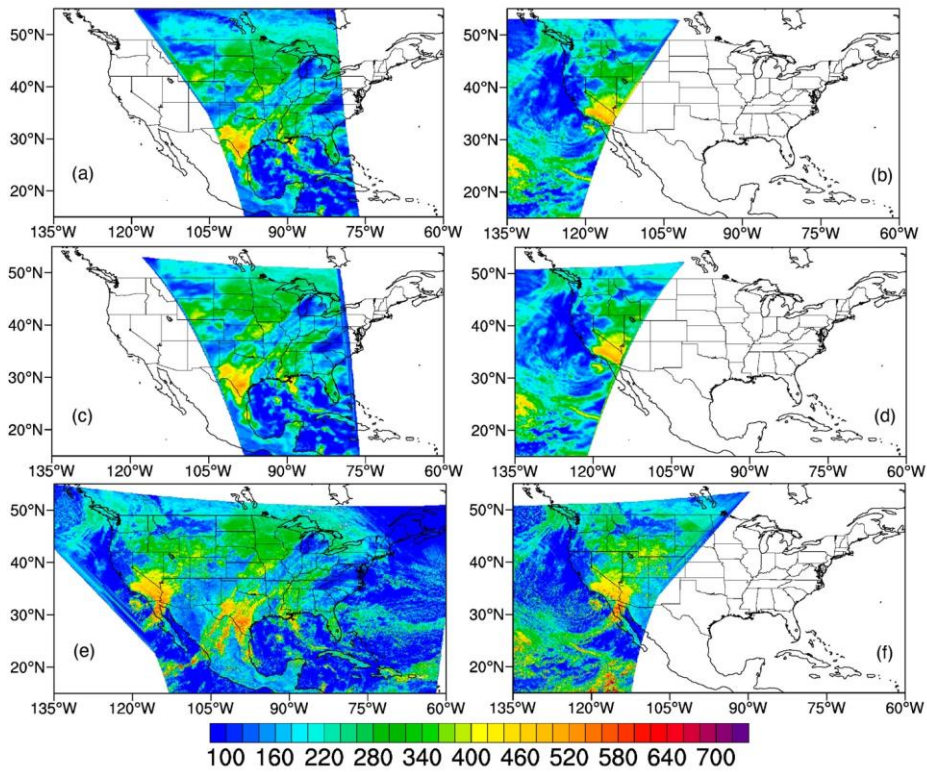
735

736

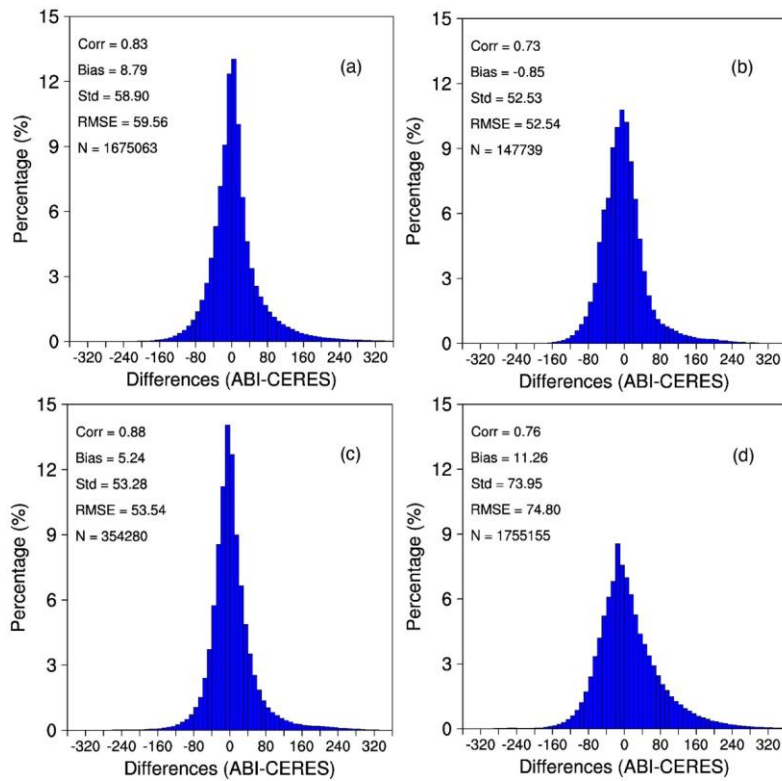
737

738

739



740
 741
 742 Figure 11. (a) All sky TOA SW from CERES_SSF/Aqua, (b) CERES_SSF/Terra, (c) re-gridded
 743 CERES_SSF/Aqua, (d) re-gridded CERES_SSF/Terra, (e) GOES-16 and (f) GOES-17
 744 on 12/26/2019 at UTC 19:36.



749

750

751

752

753

Figure 12. (a) Frequency distribution of all-sky TOA SW differences between ABI on GOES-16 and CERES, (b) ABI on GOES-17 and CERES_SSF using Aqua (Upper) and Terra (Lower). All observations were used (clear and cloudy) on 12/26/2019 at UTC 19:36.

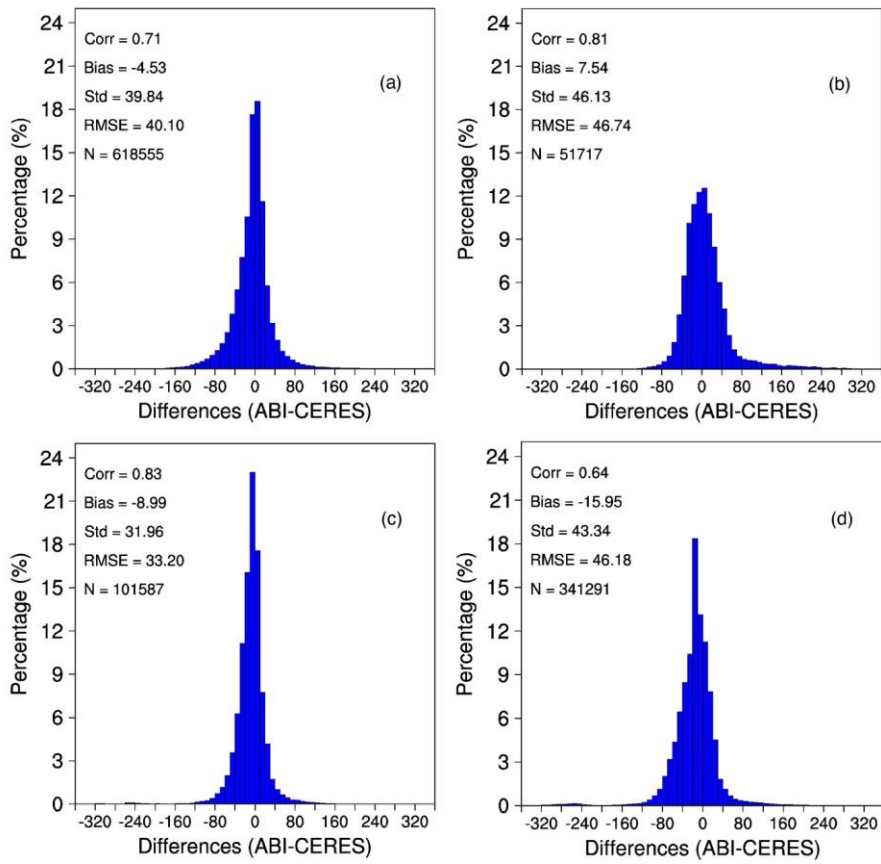


Figure 13. Same as Figure 11 but for clear TOA SW differences.

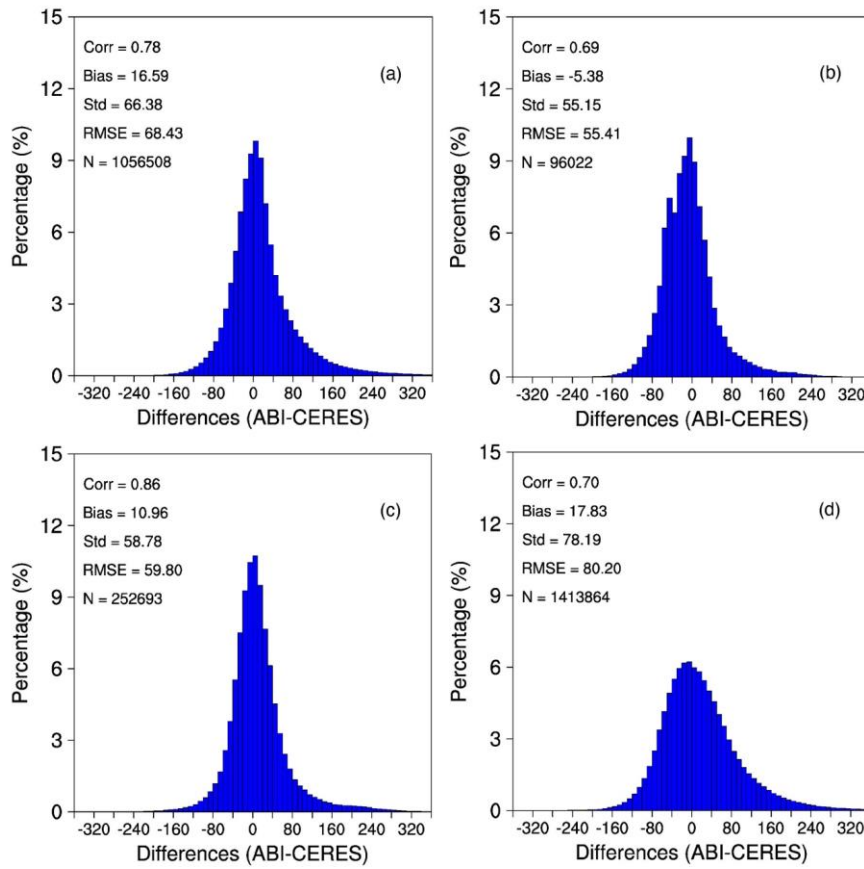
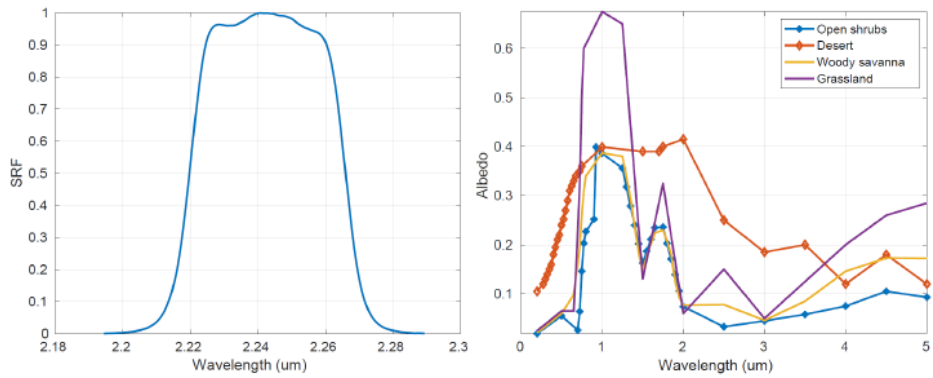


Figure 14. Same as Figure 11 but for cloudy TOA SW differences.

757
758
759
760

761



762

763 Figure 15. *Left:* Sensor response function for ABI channel 6; *Right:* Spectral albedo for desert and open
764 shrubs. Desert albedo value is much higher than open shrubs at 2.2 μm .

765

766